Article type: Full Paper

Phosphorus-Mediated MoS₂ Nanowires as a High-Performance Electrode Material for Quasi-Solid-State Sodium-Ion Intercalation Supercapacitors

Shude Liu,[1] Kwan San Hui,[2] Musheng Wu,[3] Ying Yin,[4] Kwun Nam Hui,*[5] Chu-Ying Ouyang,*[3] and Seong Chan Jun*[1]

S. Liu, Prof. K. S. Hui, Dr. M. Wu, Y. Yin, Prof. K. N. Hui, Prof. C.Y. Ouyang, Prof. S. C. Jun
[1]School of Mechanical Engineering, Yonsei University, Seoul 120-749, South Korea.
[2]School of Mathematics, University of East Anglia, Norwich, NR4 7TJ, United Kingdom.
[3]Department of Physics, Jiangxi Normal University, Nanchang, 330022, China.
[4]Guangxi Key Laboratory of Information Materials, Guilin University of Electronic Technology, Guilin 541004, PR China.
[5]Institute of Applied Physics and Materials Engineering, University of Macau, Avenida da Universidade, Taipa, Macau, China.
*Corresponding author's E-mail: bizhui@umac.mo; cyouyang@jxnu.edu.cn; scj@yonsei.ac.kr

Abstract

Molybdenum disulfide (MoS₂) is a promising electrode material for electrochemical energy storage owing to its high theoretical specific capacity and fascinating 2D layered structure. However, its sluggish kinetics for ionic diffusion and charge transfer limits its practical applications. Here, we report a promising strategy for enhancing the Na⁺ ion charge storage kinetics of MoS₂ for supercapacitors. In this strategy, electrical conductivity is enhanced and the diffusion barrier of Na⁺ ion is lowered by a facile phosphorus-doping treatment. Density functional theory results reveal that the lowest energy barrier of dilute Na-vacancy diffusion on P-doped MoS₂ (0.11 eV) is

considerably lower than that on pure MoS_2 (0.19 eV), thereby signifying prominent rate performance at high Na intercalation stages upon P-doping. Moreover, the Na-vacancy diffusion coefficient of the P-doped MoS_2 at room temperatures can be enhanced substantially by approximately two orders of magnitude (10^{-6} cm^2 s^{-1} to 10^{-4} cm^2 s^{-1}) compared with pure MoS_2. Finally, the quasi-solid-state asymmetrical supercapacitor assembled with P-doped MoS_2 and MnO_2 as the positive and negative electrode materials, respectively, exhibits an ultrahigh energy density of 67.4 W h kg^{-1} at 850 W kg^{-1} and excellent cycling stability with 93.4% capacitance retention after 5000 cycles at 8 A g^{-1}.

Keywords: phosphorus-mediated MoS_2; sodium-ion intercalation; electrochemical energy storage; quasi-solid-state supercapacitors; first-principles calculations

1. Introduction

Owing to the rapid advancement in commercial electrical device market, electrochemical energy storage systems that possess high energy and power densities have become increasingly urgent.[1, 2] Recently, supercapacitors have elicited considerable attention because they have higher energy density than traditional dielectric capacitors and greater power density and longer cyclability than rechargeable batteries.[3, 4] The charge storage and power properties of supercapacitors are usually modulated by charge storage mechanisms and the associated reaction kinetics of electrode materials.[5] Carbonaceous materials rely on electrostatic charge

accumulation at the electrode/electrolyte interface to store energy.[5] However, their relatively low energy density restricts the practical applications.[6] Alternatively, transition-metal-based materials with layered/tunneled structure (V_2O_5, MoS_2, MXene, and α-MnO_2), which are representative candidates of pseudocapacitive materials, store charge by reversible cations intercalation/deintercalation processes accompanied with fast Faradaic redox reactions at or near the active material surface, thereby providing much higher specific capacitance and energy density than carbonaceous materials.[4, 6]

Molybdenum disulfide (MoS_2), a representative transitional-metal dichalcogenide, has been actively investigated as an electrode material in electrochemical energy storage.[7-9] In the MoS_2 structure, adjacent MoS_2 layers with weak van der Waals interactions analogous to graphite possess internal space to permit the intercalation of electrolyte alkali metal ions (M = Li, Na, and K) without significant volume expansion upon cycling.[9] Interestingly, one of the unique properties of MoS_2 is that the intercalation of guest M ions within layers induces structural transition, thereby allowing the transition from hexagonal 2H semiconducting MoS_2 to tetragonal 1T metallic M_xMoS_2 and enabling enhanced electrical conductivity and rapid charge transport.[10, 11] Nevertheless, the main challenges associated with MoS_2 electrodes, such as the sluggish reaction kinetics, high energy barrier for ion intercalation and the limited number of alkali metal ions for reversible insertion/deinsertion process, restrict active material utilization.[12] These intrinsic drawbacks of MoS_2

nanostructures can be addressed by using an efficient strategy that intrinsically tune the electronic structure and increase the electrochemically active sites of MoS_2 by rational surface modification. Recent reports have shown that anion doping effectively enhances electrochemical performance by tuning the electronic structures and increasing the active sites of electroactive materials.[13-15] For instance, Liu et al.[14] demonstrated that P dopant in MoS_2 effectively improves the electrocatalytic efficiency for hydrogen evolution reaction by modifying the electronic properties and increasing active sites in the basal plane. Huang et al.[16] used a controllable P-doping strategy for synthesizing P-doped MoS_2 to significantly enhance the catalytic activities of oxygen reduction reaction; they attributed enhanced catalytic properties to the increased O_2 adsorption strength, high carrier concentration, and accelerated catalytic kinetics after the introduction of the P dopant. However, the effect of P doping into MoS_2 on the charge storage properties of supercapacitors has been rarely reported. Accordingly, the approach would be desirable if P-doping could improve the pseudocapacitance properties of MoS_2 nanostructures, thereby possibly triggering a new breakthrough in electrochemical energy storage.

We report an efficient P-doping strategy for synthesizing P-doped MoS_2 nanowires and investigate the effect of P incorporation on the pseudocapacitor performance of MoS_2 through an experimental and theoretical study. The results reveal that the incorporation of P heteroatoms into MoS_2 simultaneously induces enhanced electrical conductivity and low diffusion barrier for electrolyte Na^+ ion intercalation, thereby

increasing the capacities of nanochannels and intensifying reaction kinetics. Consequently, the resultant P-doped MoS_2 delivers a high specific capacitance of 445 F g^{-1} at 1 A g^{-1} and retains 278 F g^{-1} at 15 A g^{-1}. The quasi-solid-state asymmetric supercapacitor (ASC) using the fabricated P-doped MoS_2 as the negative electrode and MnO_2 as the positive electrode delivers an ultrahigh energy density of 67.4 W h kg^{-1} at a high power density of 850 W kg^{-1} and remarkable electrochemical cycling stability (93.4% retention after 5000 cycles at 8 A g^{-1}).

2. Results and discussion

2.1. Structural characterization and electrochemical properties of negative electrode materials

The fabrication procedure of P-doped MoS_2 nanowires is schematically presented (Figure 1a). First, ethylenediamine trimolybdate (MoO_3-EDA) inorganic–organic hybrid nanowires were synthesized with a modified low-temperature hydrothermal route.[17] Representative scanning electron microscopy (SEM) images show the uniform 1D morphology of the ~100 nm MoO_3-EDA in diameter (Figure S1a–c). The homogeneous distribution of Mo, O, C, and N elements in the MoO_3-EDA hybrid was confirmed by energy-dispersive X-ray spectroscopy (EDS; Figures S1d–i). The crystallographic structure of MoO_3-EDA was investigated by X-ray diffraction (XRD) analysis (Figure S2). All the diffraction peaks of MoO_3-EDA were well indexed to monoclinic $Mo_3O_{10}(C_6H_8N)_2$ (ICDD: 50-2402), thus matching those reported previously.[18] Second, the controllable sulfidation process was subjected to

5

solvothermal treatment at 160–200 °C (MoS$_2$-160 °C, MoS$_2$-180 °C, and MoS$_2$-200 °C). Thioacetamide is usually used as a sulfur source and reducing agent during solvothermal sulfidation. An anion-exchange reaction between S^{2-} and hybrid MoO$_3$-EDA precursor induced the formation of MoS$_3$ at the surface of a nanowire. The formed MoS$_3$ was gradually reduced to MoS$_2$, together with a transformation of the dissolution of EDA in the solvent.[19] Given the superior electrochemical performance of MoS$_2$-180 °C relative to the other MoS$_2$ (160 °C, 180 °C, and 200 °C) samples, its detailed material characterizations were discussed in the present work. The SEM images show that the surface of MoS$_2$-180 °C was wrapped by high density and flocculent nanosheets (Figures S3a, b). The hierarchical nanosheet-based MoS$_2$ nanostructure was ascribed to the imbalanced diffusion rate between the outward diffusion of the internal MoO$_3$-EDA nanowires to the outer surface of 1D hybrid precursor and the inward S^{2-} flux. The nanosheet morphology facilitates the modulation of structural deformation upon cycling.[20] The SEM image and corresponding EDS mapping of MoS$_2$-180 °C show the coexistence of Mo and S elements (Figures S3c–f). The atomic ratio of Mo/S determined by EDS spectrum was closed to the stoichiometric ratio of MoS$_2$ (Figure S3g). MoS$_2$-180 °C was used as the precursor for P-doped MoS$_2$ synthesis. In the subsequent phosphatization process, the MoS$_2$-180°C was thermally annealed in the presence of a P source under Ar flow for P-doped MoS$_2$ formation. The nanostructures of nanowires wrapped with nanosheets were retained in contrast to the nanostructures of MoS$_2$-180 °C (Figure S4a). SEM-EDS mapping analysis shows the presence of P, Mo, and S elements with an

atomic ratio of 2.69:33.79:63.52 in the P-doped MoS_2 (Figures S4b–f). The transmission electron microscopy (TEM) image shows that the P-doped MoS_2 nanowire was wrapped with thin P-doped MoS_2 nanosheets (Figure 1b), consistent with the SEM results. The unique hierarchical structure of the P-doped MoS_2 provides high density to the exposed edge sites. The MoS_2 edges presented metallic features, which may promote rapid charge transfer and enhance high electrochemical performance.[21] The N_2 adsorption–desorption isotherms of MoS_2-180 °C and P-doped MoS_2 are of type IV and showed obvious hysteresis loops (Figure S7a), thereby demonstrating the existence of mesoporous nanostructures. Pore size analysis was performed on MoS_2-180 °C and P-doped MoS_2, and the results show that the pore size centered at ~10.0 and 8.2 nm, respectively (Figure S7b). The BET surface areas and total pore volumes of MoS_2-180 °C and P-doped MoS_2 were estimated from N_2 adsorption–desorption isotherms and found to have increase from 41.2 m^2 g^{-1} to 62.9 m^2 g^{-1} and from 0.194 m^2 g^{-1} to 0.265 cm^3 g^{-1}, respectively. The findings showed that P-doping on MoS_2 efficiently increased the surface area and pore volume, thus providing additional available electrochemically active sites for charge storage. Furthermore, as shown in Figure 1c, the nanosheets with few atomic layers (5–8 layers) in their edge regions were stacked together. The interlayer spacing value was ~0.679 nm for P-doped MoS_2, exceeding the reported values for commercial MoS_2 (~0.620 nm).[22, 23] The prominent interlayer expansion exposed additional accessible active surface areas for electrolytes and lowered the energy barrier of Na^+ intercalation into the MoS_2 layers, which facilitates enhanced electrochemical Na^+

intercalation to provide superior performance.[22] The high-resolution TEM image (HRTEM) of P-doped MoS_2 showed fringes with a lattice spacing of 0.278 nm, which corresponds to the (110) plane of MoS_2 (Figure 1d). The selected area electron diffraction (SAED) pattern (Figure 1e) shows a continuous diffraction rings indexed to the (200), (100), (110), and (201) planes for the MoS_2 phase. A representative scanning TEM image and corresponding EDS elemental mappings of P-doped MoS_2 (Figures 1f–j) confirm the existence of P in the typical sample in addition to Mo and S elements. An atomic ratio of 31.74:67.03:1.23 was obtained in the corresponding EDX spectrum of Mo:S:P (Figure S5), consistent with the SEM–EDS result.

The XRD patterns in Figure S6 indicate that all the diffraction peaks of the MoS_2-180 °C are well assigned to the hexagonal 2H-MoS_2 phase (JCPDS card no. 37-1492). No extra diffraction peaks were found in P-doped MoS_2, and thus no phase transformation after P was introduced to MoS_2. However, the diffraction peak of MoS_2-180 °C and P-doped MoS_2 that corresponds to the (002) plane shifted to a lower angle than the peak of commercial bulk 2H-MoS_2. The reason is the intercalation of reactant species in the MoS_2 layers during the solvothermal process.[22] This shift expanded the interlayer spacing, which subsequently matched the interlaying spacing observed by TEM. The Raman spectrum of MoS_2-180 °C showed two characteristic peaks at 382 and 406 cm^{-1} (Figure 2a), which were indexed to the in-plane E^1_{2g} and out-of-plane A_{1g} phonon vibrational modes of 2H-MoS_2, respectively.[24] After P-doping, a broad Raman peak at around 463 cm^{-1}

corresponding to 2LA(M) mode appeared, which can be attributed to the decrease in the number of layers of P-doped MoS_2.[25, 26] The peak in the Raman spectrum for P-doped MoS_2 was blue-shifted with respect to MoS_2-180 °C (inset of Figure 2a). The shift was attributed to the presence of rich defects within P-doped MoS_2 or to the decreased unit cell of P-doped MoS_2. Moreover, the increased peak intensities of Mo-S vibration modes were ascribed to increased crystallinity due to the thermal phosphorization process. X-ray photoelectron spectroscopy (XPS) measurements were conducted for the identification of the effect of P doping on the surface chemical states in MoS_2-180 °C. Two peaks in the S 2p spectra of MoS_2-180 °C at 161.6 and 162.7 eV were attributed to S $2p_{3/2}$ and S $2p_{1/2}$ of S^{2-} species, respectively (Figure 2b).[27] For the Mo 3d XPS spectrum in MoS_2-180°C, the peaks centered at 231.9 eV (Mo $3d_{3/2}$) and 228.7eV (Mo $3d_{1/2}$) were ascribed to the appearance of Mo (IV) for characteristic MoS_2,[28] and a weak peak that corresponds to Mo^{6+} was observed (Figure 2c). The Mo 3d and S 2p peaks of P-doped MoS_2 were positively shifted because of their local chemistry changes due to P incorporation. Meanwhile, no obvious peak that corresponds to P species was observed in MoS_2-180 °C (Figure 2d), and the peaks with binding energies of 129.0 eV (P $2p_{3/2}$) and 129.8 eV (P $2p_{1/2}$) in the P 2p spectrum of P-doped MoS_2 were assigned to P that bonded to Mo ($P^{\delta-}$).[29] The peak at 133.4 eV that corresponds to surface oxidized phosphate species (P^{5+}) was due to contact with air.[30]

Figure 3a presents the cyclic voltammetry (CV) curves of the MoS_2 (160 °C, 180 °C,

and 200 °C) and P-doped MoS$_2$ electrodes at a scan rate of 20 mV s^{-1} within the potential window from −1.0 to −0.2 V (vs SCE). The P-doped MoS$_2$ showed the largest CV curve area among the samples and thus had the best energy storage capacity. Notably, the integrated area of the CV curve of nickel foam is negligible compared with the integrated areas of as-made active materials (Figure S8). Therefore, the capacitance contribution of coating substrate can be neglected. Apparently, some broad redox peaks for MoS$_2$ (160 °C, 180 °C, and 200 °C) can be found during the electrochemical process because of the intercalation/expulsion of Na$^+$ ions between MoS$_2$ layers.[31, 32] To further study the charge storage mechanism in electrode materials, ex-situ XRD of P-doped MoS$_2$ electrode at different cut-off potentials was performed (Figure S9). The (002) peak of the initial P-doped MoS$_2$ was shifted toward lower angle and the peak density also decreased when the electrode was charged to −0.3 V (vs SCE). The finding implies the lattice expansion along the c-axis, which results from the increase of interlayer spacing after Na$^+$ intercalation. Notably, the (002) peak was shifted back to original state (2θ ≈ 13.4°) when discharged to −1.0 V (vs SCE), indicating good reversibility of the intercalation/de-intercalation behavior of P-doped MoS$_2$. Figure S10a exhibits CV curves of the P-doped MoS$_2$ electrodes at various scan rates at 5–50 mV s^{-1}. Given the increasing scan rates, similar CV curve shapes remained. This result suggests that P-doped MoS$_2$ has a good electrochemical behavior and fast charge/discharge property.[33]

Figure 3b compares galvanostatic charge/discharge (GCD) curves of MoS$_2$ (160 °C,

180 °C, and 200 °C) and P-doped MoS_2 electrodes performed from −1.0 to −0.3 V (vs

SCE) at a current density of 1 A g^{-1}. As expected, the P-doped MoS_2 showed a longer

discharge time than MoS_2 (160 °C, 180 °C, and 200 °C). This result indicates that the

introduction of P into MoS_2 accelerates the reaction kinetics. The presence of

potential plateaus observed in the GCD curves of as-synthesized materials revealed

their typical pseudocapacitive properties involving with Na^+

intercalation/deintercalation behaviours.[34] The nearly symmetrical GCD curves of

P-doped MoS_2 at different current densities confirm the high reversibility of electrode

material (Figure S10b).[35] The specific capacitance of P-doped MoS_2 reaches up to

445 F g^{-1} at a current density of 1 A g^{-1} (Figure 3c), which is higher than values of

MoS_2-160 °C (305 F g^{-1}), MoS_2-180 °C (376 F g^{-1}), and MoS_2-200 °C (335 F g^{-1}).

This specific capacitance of P-doped MoS_2 surpasses the previously reported values

of MoS_2 nanostructures and MoS_2-based systems.[36-40] As the current density is

increased to 15 A g^{-1}, the P-doped MoS_2 demonstrates the best rate capability and still

maintains the specific capacitance of 278 F g^{-1}, which is substantially higher than the

values of MoS_2-160 °C (101 F g^{-1}), MoS_2-180 °C (178 F g^{-1}), and MoS_2-200 °C

(137 F g^{-1}).

We conducted electrochemical impedance spectroscopy (EIS) to investigate the

electrochemical performance characteristics of MoS_2 (160 °C, 180 °C, and 200 °C)

and P-doped MoS_2 investigate electrochemical performance characteristics of MoS_2

(160 °C, 180 °C, and 200 °C) and P-doped MoS_2. As presented in Figure S11, the

Nyquist plots show that all the samples have two distinct parts, including a semicircle associated with Faradaic charge-transfer resistance (R_{ct}) and a straight slope related to diffusion-limited resistance.[41] The intersection between the plot and real axis of the semicircle is related to the equivalent series resistance (R_s), which consists of the electrolyte resistance, contact resistance, and intrinsic resistance of the electrode.[42] The P-doped MoS_2 shows smaller resistance (R_s = 2.5 Ω, R_{ct} = 22.6 Ω) than MoS_2 (160 °C, 180 °C, and 200 °C) and thus shows enhanced electrical conductivity and charge transfer property after P incorporation. The slope of a straight line along the imaginary axis at a low frequency region for P-doped MoS_2 is steeper compared with that of MoS_2 (160 °C, 180 °C, and 200 °C), thereby revealing a faster electrolyte diffusion rate in P-doped MoS_2.[43] These results are attributed to the partial replacement of S with P on the surface. This partial replacement remarkably improves the electrical conductivity of P-doped MoS_2 and facilitates the interface charge transfer and fast diffusion of electrolyte ions. The electrical properties of samples were examined by a four-point probe configuration. As expected, the electrical conductivity of P-doped MoS_2 (2.9×10^{-3} S cm^{-1}) has significantly improved relative to that of MoS_2-180 °C (4.6×10^{-4} S cm^{-1}). The reactive property of electrode materials is relevant to the covalent-ionic bond character, which can be evaluated by the equation of covalent character (%)=$\exp[-0.25(X_a-X_b)^2]$,[44] (where X_a and X_b are electronegativity values of cation and anion, respectively). The ratios of covalent bonds in Mo-S and Mo-P are determined to 95.69% and 99.98%, respectively (X_{Mo} = 2.16, X_S = 2.58, and X_P = 2.19 Pauling units). The higher the covalent character of

P-doped MoS$_2$ is, the lower the weak attraction to electrons in Mo 3d orbital is.[45] Thus, the migration energy of electrons decreases, and surface redox reactivity is enhanced during the electrochemical process.

The cycling performances of MoS$_2$ (160 °C, 180 °C, and 200 °C) and P-doped MoS$_2$ were investigated with consecutive GCD test at a current density of 5 A g^{-1}. The results are shown in Figure 3d. The P-doped MoS$_2$ shows good cycling stability with 90.6% retention of the initial capacitance after 5000 cycles. By contrast, the capacitance retention rates of MoS$_2$-160 °C, MoS$_2$-180 °C, and MoS$_2$-200 °C are 83.9%, 87.1%, and 85.2%, respectively, after the same operation. The achieved cycling performance of P-doped MoS$_2$ exceeds the cycling performance of MoS$_2$-based materials reported in the literature.[33, 46, 47] The excellent electrochemical performance of P-doped MoS$_2$ may be attributed to the peculiar anisotropy of 1D nanowires associated to fast ion transport and formed 2D nanosheets on the surface of nanowire-related short ion diffusion path and to the rich Faradaic electrochemistry after P-doping.[20, 48, 49] To examine the structural stability of P-doped MoS$_2$, we conducted TEM analysis of P-doped MoS$_2$ after 5000 cycles. The clear 1D nanostructure and edge-terminated features are retained (Figure S12a, b), thereby indicating its good structural integrity. The interlayer spacing of P-doped MoS$_2$ shows an obvious increase from ~0.679 nm to ~0.780 nm after a cycling test (Figure S12c, d). The expanded interlayer spacing is due to the repetition of Na$^+$ insertion and extraction upon cycling and provides many active reaction sites for Na$^+$ storage and a

13

low energy barrier for ion intercalation,[22] thereby further contributing to high Na^+ storage properties of active materials.

2.2. Density functional theory (DFT) calculations

To probe the effect of P-doping on the electrochemical performance of MoS_2, we carried out systematic DFT calculations. The structural models of pure MoS_2 and P-doped MoS_2 are presented in Figure S13. Figures 4a and b show the electronic structures of $2H\text{-}MoS_2$ before and after P-doping, respectively. Pure $2H\text{-}MoS_2$ exhibits obvious semiconducting characteristics with a band gap of 1.68 eV. After P-doping, the Fermi level merges into the valence band, thereby resulting in the metallic property of P-doped MoS_2. Thus, the electrical conductivity of P-doped MoS_2 increases compared with that of pure MoS_2, consistent with the experimental results (Figure S11). Na^+ intercalation concentration on MoS_2 is closely related with charge storage capability. Basing on the stable intercalation sites of Na^+ ion, we calculated the formation energy (E_f, the definition can be seen in Supporting Information) of Na^+ ion on pure MoS_2 and P-doped MoS_2. We found that energy formation can be improved substantially after P-doping, and P-doped MoS_2 can accommodate up to four Na ions per formula unit, whereas pure MoS_2 can only accommodate up to three Na ions per formula unit, as shown in Figures 4c and d. Accordingly, P-doping is beneficial to the intercalation of Na^+ ions on the MoS_2 basal plane and improves the specific capacitance of P-doped MoS_2. The ion diffusion kinetics directly determines the rate capability of pseudocapacitors. From the

theoretical perspective, the energy barrier of ion diffusion can reflect the reaction kinetics of MoS_2. Therefore, we investigated the diffusion barrier of Na^+ ions on pure MoS_2 and P-doped MoS_2. Two extreme cases (dilute Na-ion diffusion modeled with one Na ion on MoS_2 supercell and dilute Na-vacancy diffusion modeled by creating one Na-vacancy in the fully Na-adsorbed MoS_2 supercell) are considered in our calculations, thereby corresponding to the Na-deintercalated stage and Na-intercalated stage, respectively. For a moderate Na-concentration, the Na^+ ion diffusion energy barrier should be between the above two extreme cases. Figures 4e and f show the energy profiles of dilute Na-ion diffusion on MoS_2 with and without P-doping; the corresponding diffusion paths are shown in the inset. Diffusion path 2 is a thermodynamically favorable migration path for Na^+ ion on pure MoS_2. For P-doped MoS_2, the diffusion barrier along path 2 is lowest among the available diffusion paths. The lowest diffusion barrier of Na ions on P-doped MoS_2 (0.10 eV) is extremely low, although slightly higher compared with that on pure MoS_2 (0.088 eV). At low Na ion diffusion energy barriers, the magnitude of diffusion coefficients is $\sim 10^{-4}$ cm^2 s^{-1} for both MoS_2 and P-doped MoS_2 at room temperature (Table S3). Given the extremely large diffusion coefficient for dilute Na-ion diffusion, the rate of performance in the Na-deficient stage would be governed by the electrical conductivity of active materials. The enhanced electrical conductivity of P-doped MoS_2 may improve rate performance. When the Na^+ intercalation concentration is high, Na^+ diffusion can be regarded as the vacancy diffusion along the opposite direction. Figures 4g and h show the energy profiles of dilute Na-vacancy diffusion on MoS_2 with and without

P-doping. Obviously, the lowest energy barrier of dilute Na-vacancy diffusion on P-doped MoS_2 (0.11 eV) is significantly lower than that on pure MoS_2 (0.19 eV), thereby showing that rate performance can be improved substantially at high Na intercalation stages upon P-doping. Thus, the Na-vacancy diffusion coefficient of the MoS_2 at room temperatures can be enhanced substantially by approximately two orders of magnitude (from 10^{-6} cm^2 s^{-1} to 10^{-4} cm^2 s^{-1}, as shown in Table S3). The low energy barrier and high diffusion coefficient of Na^+ ion on P-doped MoS_2 facilitate Na^+ efficient insertion and extraction, thereby boosting the pseudocapacitive process for Na^+ storage. Overall, following the DFT calculations, the electrochemical performance of P-doped MoS_2 is efficiently improved relative to that of pure MoS_2, thereby further confirming our experimental results.

2.3. Structural characterization and electrochemical properties of positive electrode materials

MnO_2 has been considered a promising positive electrode material for supercapacitors owing to its reversible cation intercalation/deintercalation process that accompanies fast redox reaction of Mn^{3+}/Mn^{4+}.[50] These properties accounts for the high theoretical specific capacitance and wide working potential window MnO_2. Herein, MnO_2 was prepared by a facile hydrothermal route involving the redox reaction of $2MnO_4^- + 3Mn^{2+} + 2H_2O \rightarrow 5MnO_2 + 4H^+$ (details in experimental section). SEM images in Figures S14a and b show that the MnO_2 microstructure is composed of nanorods with an average diameter of $\sim$40 nm. The SEM-EDS mapping images

show that Mn and O elements are uniformly distributed in the entire MnO_2 (Figures S14c–f). The XRD pattern of MnO_2 (Figure S15a) can be indexed into α-MnO_2 phase (JCPDS card no. 44-0141). The Raman spectrum of MnO_2 shows the peaks at 183, 389, 576, and 642 cm^{-1} (Figure S15b), thereby agreeing with the literature report for α-MnO_2.[51] The CV curves of MnO_2 recorded at different scan rates show quasi-rectangular shapes in 1 M Na_2SO_4 electrolyte (Figure S16a), indicating good capacitive-like electrochemical properties. The specific capacitance of MnO_2 calculated from the GCD curve is 339 F g^{-1} at the current density of 1 A g^{-1} and still retains 251 F g^{-1} even at a high current density of 10 A g^{-1} (Figure S16b).

2.4. Electrochemical performance of the quasi-solid-state P-doped MoS₂//MnO₂ ASC device

Aqueous electrolytes are commonly used in most reported supercapacitors because of their high-ionic conductivity and low cost.[52] However, the possible leakage of harmful electrolytes inevitably causes fast capacity fading in operation.[53] By comparison, all-solid-state electrolytes overcome the issue and achieve large cell voltage because they are not limited by thermodynamic stability.[54] Accordingly, quasi-solid-state electrolytes are desirable in integrating the advantages of rapid ions transmission of aqueous electrolyte and high stability of all-solid-state electrolytes. To evaluate the superior electrochemical properties of the P-doped MoS_2 for practical application, we assembled a quasi-solid-state ASC device with as-fabricated P-doped MoS_2 as the negative electrode and MnO_2 as the positive electrode, using polyvinyl

alcohol (PVA)/Na$_2$SO$_4$ gel electrolyte (Figure 5a). To achieve the optimal performance

of the ASC device, the mass ratio of MnO$_2$ to P-doped MoS$_2$ was determined as ~0.67

in the device in the condition of scan rate conducted at 20 mV s^{-1} for both electrodes

(Figure 5b).

Figure 5c shows the CV curves of P-doped MoS$_2$//MnO$_2$ ASC device at different

voltage windows at a scan rate of 10 mV s^{-1}. As expected, the stable operating voltage

of the device can be extended up to 1.7 V. All the CV curves show quasi-rectangular

shapes with a wide hump (Figure 5d), thereby indicating that the charge contribution

originates from Faradaic and non-Faradaic reactions. The shapes of CV curves output

with the minimal change as the scan rate magnifies, suggesting the high reversibility

and superior rate capability of the device.[55] The symmetric GCD curves (Figure 5e)

with triangular shapes reflects the rapid $I-V$ response of our assembled device. The

specific capacitances based on the discharge curves were plotted as a function of

current density (Figure S17). The device achieves a specific capacitance of 168 F g^{-1}

at a current density of 1 A g^{-1}. Notably, the device exhibits a prominent rate

performance with a specific capacitance of 57 F g^{-1} at a high current density of

16 A g^{-1}. The cycling performance was measured at a high current density of 8 A g^{-1}

for 5000 continuous GCD cycles (Figure 5f). Specific capacitance at approximately

3200 cycles increases because of the electroactivation of P-doped MoS$_2$ by

continuous intercalation/deintercalation of Na$^+$ into the interlayer lattice of MoS$_2$ to

form Na$_x$MoS$_2$.[10, 11] Nearly 93.4% of the initial capacitance with high Coulombic

efficiency of 97.1% is retained after the cyclic test, considerably exceeding the

capacitance retentions of previously reported ASC devices.[41, 48, 56, 57] The R_s and R_{ct} of the device obtained from EIS plot before cycling are 3.4 and 36.8 Ω, respectively (Figure S18). After the cycling test, the resistance values estimated from Nyquist plots slightly increase, which is possibly attributed to the loss of adhesion of the active materials within the current collector that impedes the diffusion pathways of ions during cycling. The energy and power densities of the device calculated from GCD curves were presented as the Ragone plot in comparison with recently reported ASC devices (Figure 5g). The device delivers a high energy density of 67.4 W h kg^{-1} at a power density of 850 W kg^{-1}, while it still maintains a decent energy density of 22.5 W h kg^{-1} at a high power density of 13 600 W kg^{-1}. The high energy and power densities obtained here are superior to the values reported for most of ASC devices, including nickel sulfides/MoS$_2$/CNT//AC,[58] MoS$_2$/graphene foam//AC,[59] MoS$_2$/NiCo$_2$O$_4$//AC,[60] MoS$_2$/rGO//MnO$_2$/rGO,[61] MoO$_3$@CNT//MnO$_2$@CNT,[62] and MnO$_2$//activated rGO.[63] To demonstrate the availability of energy output for our device, we integrated two assembled devices in parallel or series connections. This approach increases total capacitance or output voltage (Figure 5h). As a proof of concept, two charged P-doped MoS$_2$//MnO$_2$ devices in series were used to power a red light-emitting diode (LED; ~2V; Figure 5i). The P-doped MoS$_2$ shows excellent performance and thus holds great potential in the development of advanced electrode materials for electrochemical energy storage.

3. Conclusions

We demonstrate an efficient P-anion modification strategy for boosting the electrochemical performance of P-doped MoS_2 nanowires. The results of the experimental and theoretical study show that the P dopant in MoS_2 creates newly formed active sites, decreases the diffusion barrier of Na^+ ions, and promotes the intrinsic electrical conductivity, thereby resulting in significantly improved reaction kinetics for Na^+ intercalation. The P-doped MoS_2 delivers a high specific capacitance of 445 F g^{-1} at a current density of 1 A g^{-1}, and still maintains 278 F g^{-1} even at a high current density of 15 A g^{-1}. Furthermore, the quasi-solid-state ASC device that uses P-doped MoS_2 and MnO_2 achieves an ultrahigh energy density of 67.4 W h kg^{-1} at a power density of 850 W kg^{-1}, while retaining a value of 22.5 W h kg^{-1} under a high power density of 13 600 W kg^{-1}. Furthermore, the device delivers excellent cycling stability with capacitance retention of 93.4% after 5000 cycles. The original concept of our work can be used for rationally constructing advanced electrode materials for electrochemical energy storage.

Supporting Information

Supporting Information is available from the Wiley Online Library or from the author.

Conflicts of interest

The authors declare there are no conflicts of interest.
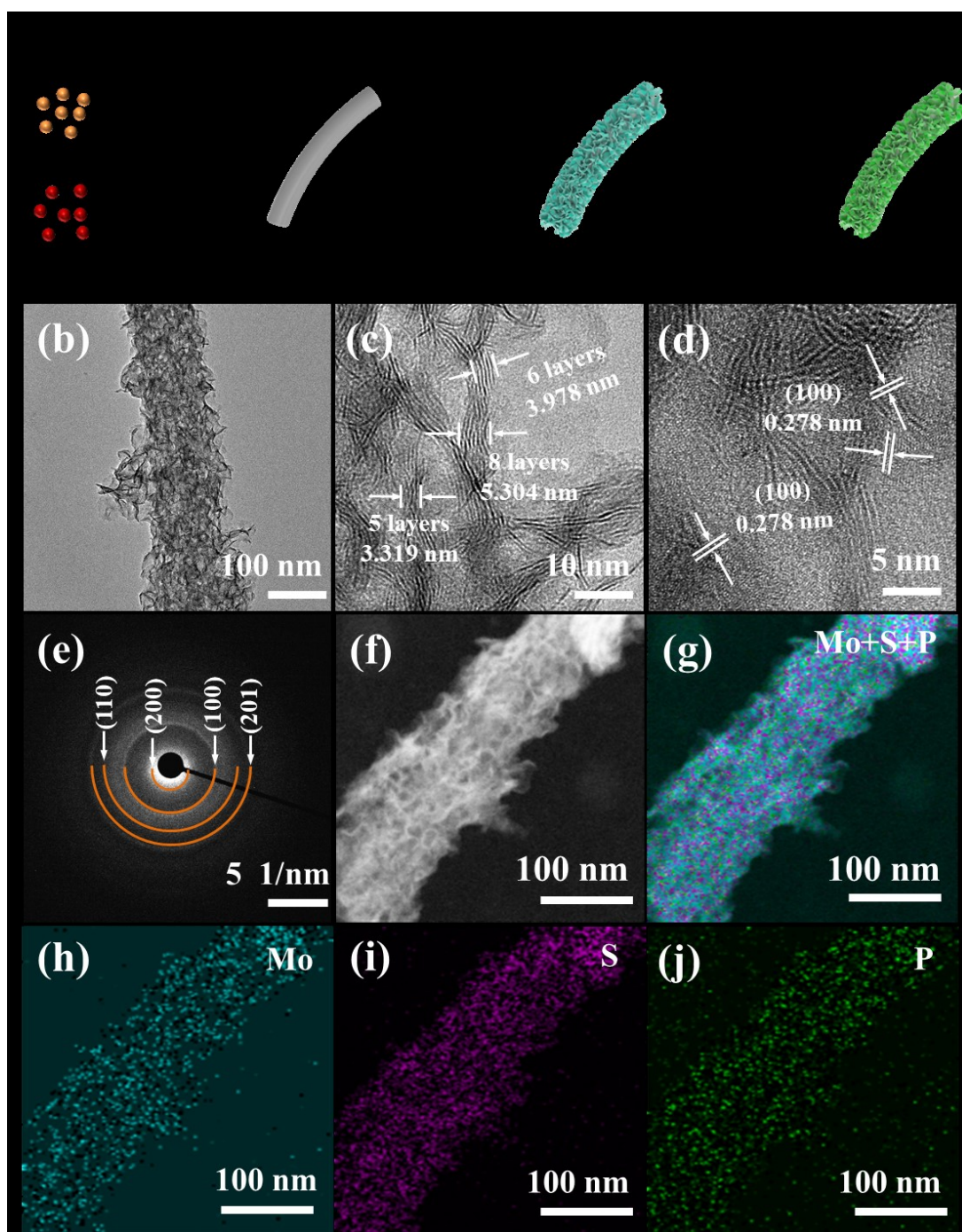
Figure 1. (a) Schematic illustration of the preparation of P-doped MoS$_2$ nanowires. (b, c) TEM images, (d) HRTEM image, (e) SAED pattern, and (f–j) TEM-EDS elemental mapping images of P-doped MoS$_2$ nanowires.
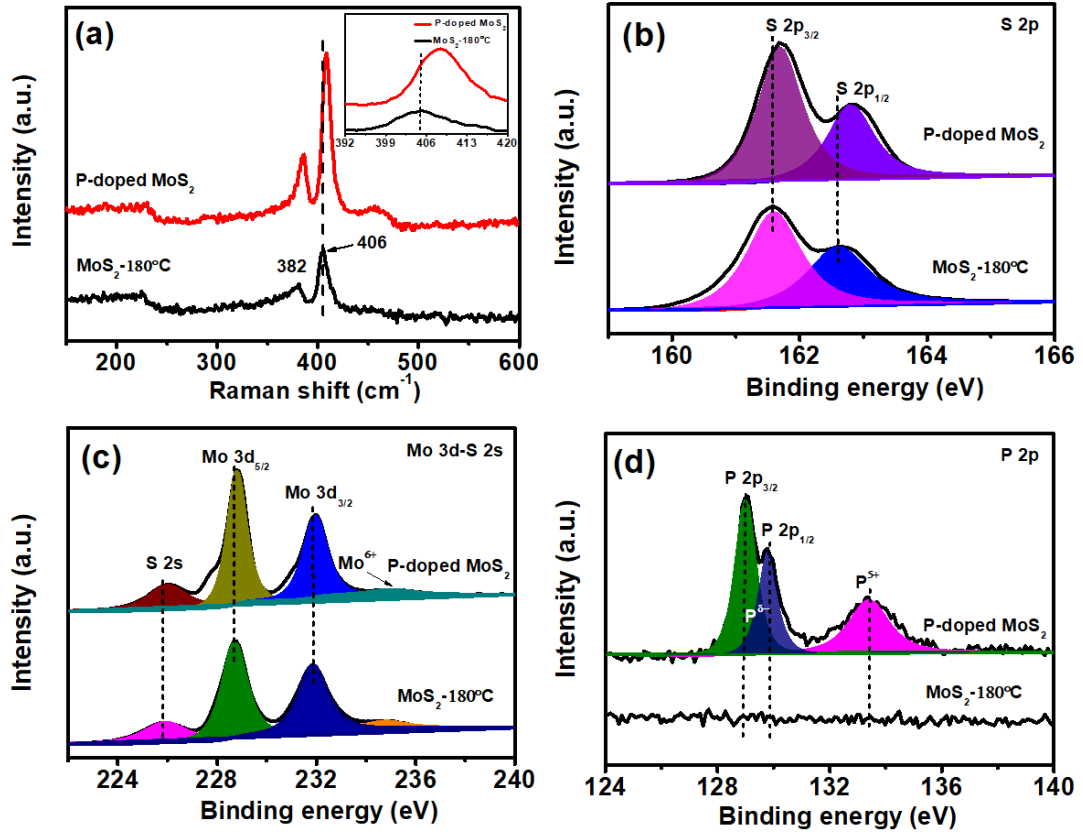
Figure 2. (a) Raman spectra for MoS$_2$-180 °C and P-doped MoS$_2$ samples. XPS spectra of (b) S 2p, (c) Mo 3d–S 2s, and (d) P 2p for MoS$_2$-180 °C and P-doped MoS$_2$ samples.
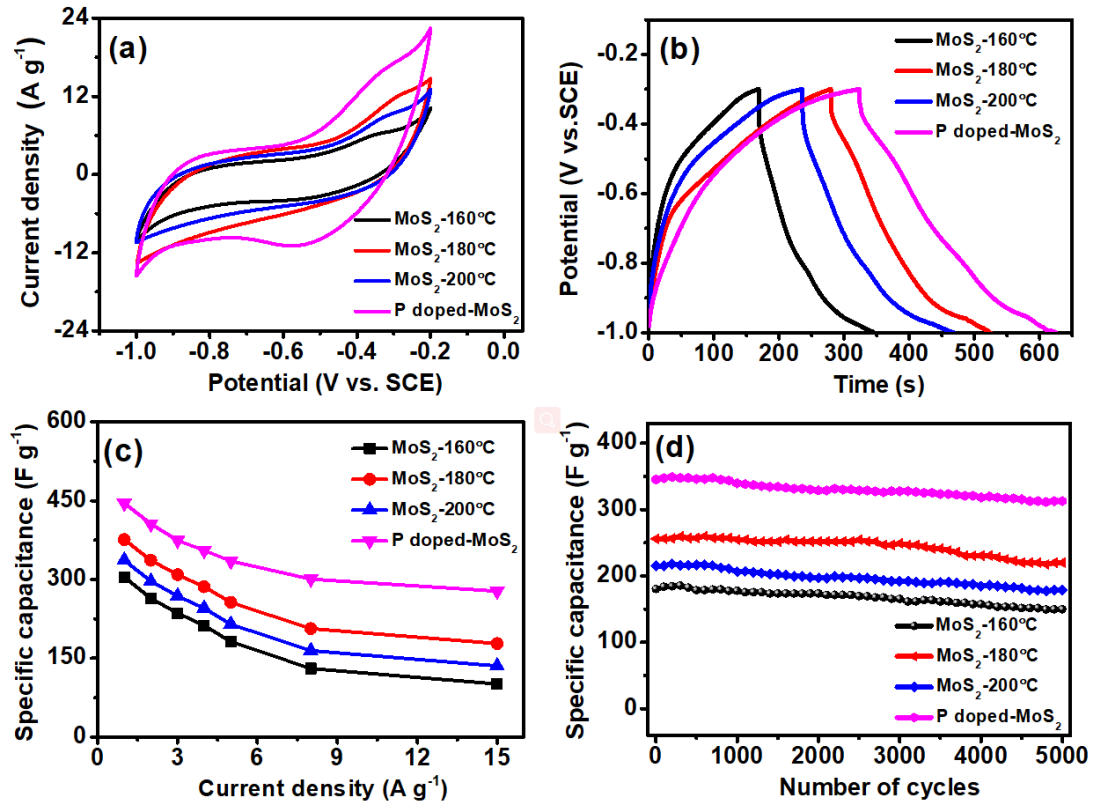
Figure 3. (a) Comparative CV curves of MoS_2 (160, 180 and 200 °C) and P-doped MoS_2 at a scan rate of 20 mV s^{-1}. (b) Comparative GCD curves of MoS_2 (160 °C, 180 °C, and 200 °C) and P-doped MoS_2 at a current density of 1 A g^{-1}. (c) Specific capacitance vs. different current densities for MoS_2 (160 °C, 180 °C, and 200 °C) and P-doped MoS_2. (c) Cycling performances of MoS_2 (160 °C, 180 °C, and 200 °C) and P-doped MoS_2 at a current density 5 A g^{-1} for 5000 cycles.

23
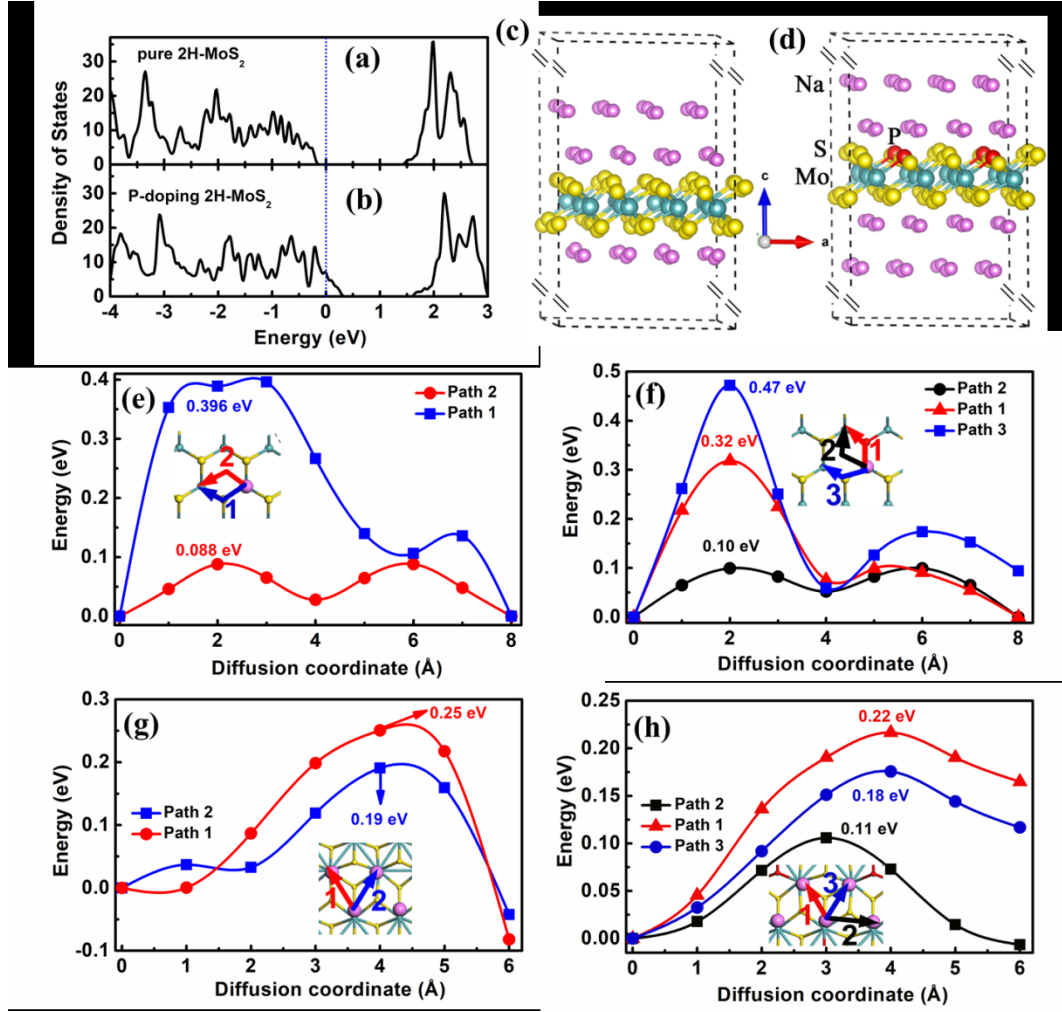
Figure 4. Density of states of (a) $2H\text{-}MoS_2$ and (b) P-doped MoS_2. Intercalation configurations of Na^+ ions on (c) pure MoS_2 and (d) P-doped MoS_2 with the largest intercalation concentration. Energy profiles of Na^+ ion diffusion on (e) pure MoS_2 and (f) P-doped MoS_2. Energy profiles of vacancy diffusion on (g) pure MoS_2 and (h) P-doped MoS_2. Possible diffusion paths are correspondingly shown in the inset of (e–h).
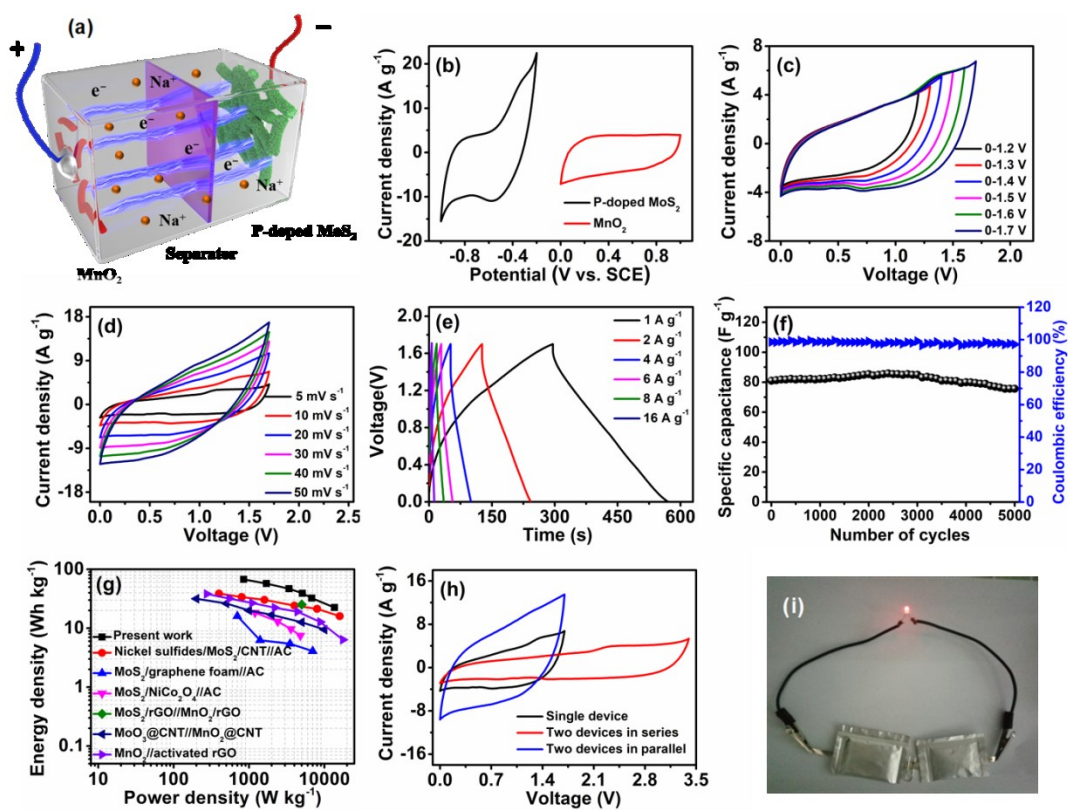
Figure 5. Electrochemical performances of quasi-solid-state P-doped MoS_2//MnO_2 ASC device. (a) Schematic illustration of assembled structure of the device. (b) Comparative CV curves obtained for P-doped MoS_2 and MnO_2 at a scan rate of 20 mV s^{-1}. (c) CV curves of the device in different operating voltages at a scan rate of 10 mV s^{-1}. (d) CV curves of the device at different scan rates. (e) GCD curves of the device at various current densities. (f) Cycling performance and Coulombic efficiency of the device at a high current density of 8 A g^{-1}. (g) Ragone plots of the device along with recently reported ASCs for comparison. (h) CV curves of the assembled devices connected in series and in parallel at a scan rate of 10 mV s^{-1}. (i) Photograph of two charged devices connected in series power up a red LED.

Graphical abstract
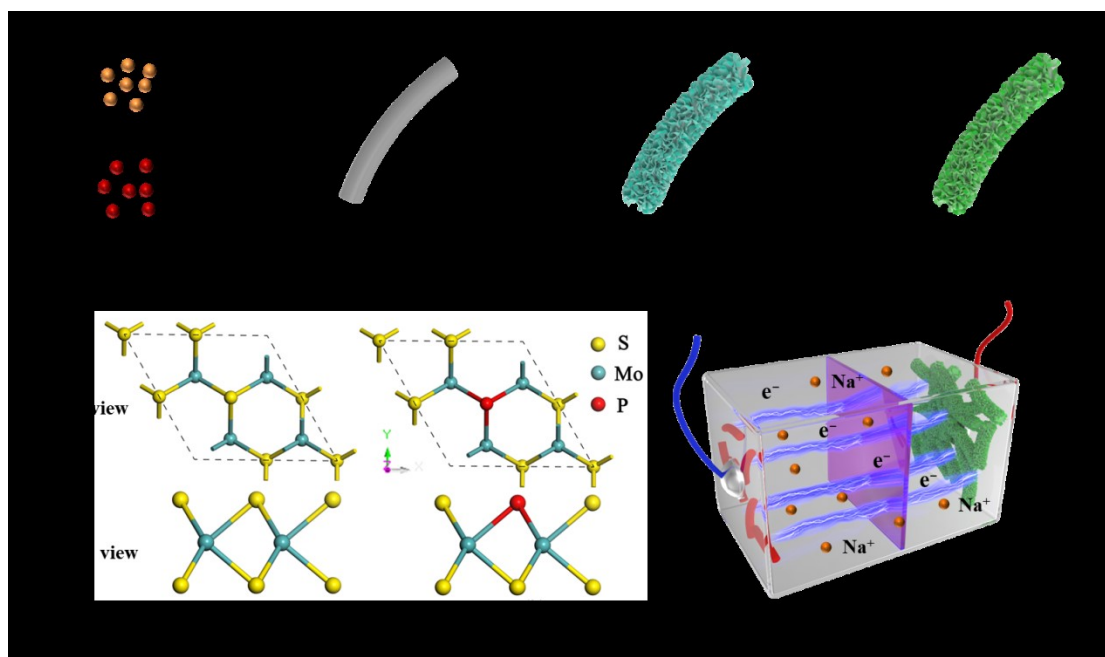
We proposed an efficient P-anion doping strategy to realize the synergistic regulation toward the number of electrochemical active sites, electrical structure, and energy barrier of Na^+ ion diffusion in MoS_2 nanowires through a combined experimental and first-principles study. The resultant P-doped MoS_2 shows significantly enhanced electrochemical performance, exhibiting higher specific capacitance and rate capability than pristine MoS_2. Quasi-solid-state asymmetric supercapacitor devices that use P-doped MoS_2 anode and MnO_2 cathode achieve a high energy density (67.4 W h kg^{-1}) at 850 W kg^{-1} and deliver excellent cycling stability that retains 93.4% of initial capacitance after 5000 cycles.

References

1. Shen, L.; Lv, H.; Chen, S.; Kopold, P.; van Aken, P. A.; Wu, X.; Maier, J.; Yu, Y., *Adv. Mater.* **2017,** *29* (27), 1700142.

2. Chen, S.; Wu, F.; Shen, L.; Huang, Y.; Sinha, S. K.; Srot, V.; van Aken, P. A.; Maier, J.; Yu, Y., *ACS Nano* **2018,** *12* (7), 7018-7027.

3. Dong, S.; Shen, L.; Li, H.; Pang, G.; Dou, H.; Zhang, X., *Adv Funct Mater.* **2016,** *26* (21), 3703-3710.

4. Hou, L.; Shi, Y.; Wu, C.; Zhang, Y.; Ma, Y.; Sun, X.; Sun, J.; Zhang, X.; Yuan, C., *Adv Funct Mater.* **2018,** *28* (13), 1705921.

5. Jiang, Q.; Kurra, N.; Alhabeb, M.; Gogotsi, Y.; Alshareef, H. N., *Adv. Energy Mater.* **2018,** *8* (13), 1703043.

6. Li, J.; Yuan, X.; Lin, C.; Yang, Y.; Xu, L.; Du, X.; Xie, J.; Lin, J.; Sun, J., *Adv. Energy Mater.* **2017,** *7* (15), 1602725.

7. Wang, S.; Guan, B. Y.; Yu, L.; Lou, X. W., *Adv. Mater.* **2017,** *29* (37), 1702724.

8. Zhang, Y.; Sun, W.; Rui, X.; Li, B.; Tan, H. T.; Guo, G.; Madhavi, S.; Zong, Y.; Yan, Q., *Small* **2015,** *11* (30), 3694-3702.

9. Zhu, J.; Sun, W.; Yang, D.; Zhang, Y.; Hoon, H. H.; Zhang, H.; Yan, Q., *Small* **2015,** *11* (33), 4123-4129.

10. Lin, Y.-C.; Dumcenco, D. O.; Huang, Y.-S.; Suenaga, K., *Nat. Nanotechnol.* **2014,** *9* (5), 391.

11. Kochat, V.; Apte, A.; Hachtel, J. A.; Kumazoe, H.; Krishnamoorthy, A.; Susarla, S.; Idrobo, J. C.; Shimojo, F.; Vashishta, P.; Kalia, R., *Adv. Mater.* **2017,** *29* (43), 1703754.

12. Wang, G.; Zhang, J.; Yang, S.; Wang, F.; Zhuang, X.; Müllen, K.; Feng, X., *Adv. Energy Mater.* **2018,** *8* (8), 1702254.

13. Azcatl, A.; Qin, X.; Prakash, A.; Zhang, C.; Cheng, L.; Wang, Q.; Lu, N.; Kim, M. J.; Kim, J.; Cho, K., *Nano Lett.* **2016,** *16* (9), 5437-5443.

14. Liu, P.; Zhu, J.; Zhang, J.; Xi, P.; Tao, K.; Gao, D.; Xue, D., *ACS Energy Lett.* **2017,** *2* (4), 745-752.

15. Yu, M.; Wang, Z.; Hou, C.; Wang, Z.; Liang, C.; Zhao, C.; Tong, Y.; Lu, X.; Yang, S., *Adv. Mater.* **2017,** *29* (15), 1602868.

16. Huang, H.; Feng, X.; Du, C.; Song, W., *Chem comm* **2015,** *51* (37), 7903-7906.

17. Zhuo, S.; Xu, Y.; Zhao, W.; Zhang, J.; Zhang, B., *Angew. Chem. Int. Ed.* **2013,** *125* (33), 8764-8768.

18. Gao, Q.; Wang, S.; Fang, H.; Weng, J.; Zhang, Y.; Mao, J.; Tang, Y., *J. Mater. Chem.* **2012,** *22* (11), 4709-4715.

19. Chen, S.-A.; Hwang, G.-W., *J. Am. Chem. Soc.* **1995,** *117* (40), 10055-10062.

20. Chen, Y. M.; Yu, X. Y.; Li, Z.; Paik, U.; Lou, X. W. D., *Sci. Adv* **2016,** *2* (7), e1600021.

21. Xiao, W.; Liu, P.; Zhang, J.; Song, W.; Feng, Y. P.; Gao, D.; Ding, J., *Adv. Energy Mater.* **2017,** *7* (7), 1602086.

22. Hu, Z.; Wang, L.; Zhang, K.; Wang, J.; Cheng, F.; Tao, Z.; Chen, J., *Angew. Chem. Int. Ed.* **2014,** *53* (47), 12794-12798.

23. Zhao, C.; Yu, C.; Zhang, M.; Sun, Q.; Li, S.; Banis, M. N.; Han, X.; Dong, Q.; Yang, J.; Wang, G., *Nano Energy* **2017,** *41*, 66-74.

24. Xie, X.; Makaryan, T.; Zhao, M.; Van Aken, K. L.; Gogotsi, Y.; Wang, G., *Adv. Energy Mater.* **2016,** *6* (5), 1502161.

25. Wang, Y.; Cong, C.; Qiu, C.; Yu, T., *Small* **2013,** *9* (17), 2857-2861.

26. Berkdemir, A.; Gutiérrez, H. R.; Botello-Méndez, A. R.; Perea-López, N.; Elías, A. L.; Chia, C.-I.; Wang, B.; Crespi, V. H.; López-Urías, F.; Charlier, J.-C., *Sci. Rep.* **2013,** *3*, 1755.

27. Zhao, W.; Liu, Y.; Wei, Z.; Yang, S.; He, H.; Sun, C., *Appl Catal B.* **2016,** *185*, 242-252.

28. Huang, L. B.; Zhao, L.; Zhang, Y.; Chen, Y. Y.; Zhang, Q. H.; Luo, H.; Zhang, X.; Tang, T.; Gu, L.; Hu, J. S., *Adv. Energy Mater.* **2018,** *8* (21), 1800734.

29. Wang, Z.; Liu, H.; Ge, R.; Ren, X.; Ren, J.; Yang, D.; Zhang, L.; Sun, X., *ACS Catal.* **2018,** *8*, 2236-2241.

30. Liang, H.; Xia, C.; Jiang, Q.; Gandi, A. N.; Schwingenschlögl, U.; Alshareef, H. N., *Nano Energy* **2017,** *35*, 331-340.

31. Bissett, M. A.; Kinloch, I. A.; Dryfe, R. A., *ACS Appl. Mater. Interfaces* **2015,** *7* (31), 17388-17398.

32. Lee, J.-S. M.; Briggs, M. E.; Hu, C.-C.; Cooper, A. I., *Nano Energy* **2018,** *46*, 277-289.

33. Tang, H.; Wang, J.; Yin, H.; Zhao, H.; Wang, D.; Tang, Z., *Adv. Mater.* **2015,** *27* (6), 1117-1123.

34. Zhou, J.; Qin, J.; Zhang, X.; Shi, C.; Liu, E.; Li, J.; Zhao, N.; He, C., *ACS Nano* **2015,** *9* (4), 3837-3848.

35. Qin, L.; Tao, Q.; El Ghazaly, A.; Fernandez-Rodriguez, J.; Persson, P. O.; Rosen, J.; Zhang, F., *Adv Funct Mater.* **2018,** *28* (2), 1703808.

36. Yang, Y.; Fei, H.; Ruan, G.; Xiang, C.; Tour, J. M., *Adv. Mater.* **2014,** *26* (48), 8163-8168.

37. Cao, L.; Yang, S.; Gao, W.; Liu, Z.; Gong, Y.; Ma, L.; Shi, G.; Lei, S.; Zhang, Y.; Zhang, S., *Small* **2013,** *9* (17), 2905-2910.

38. da Silveira Firmiano, E. G.; Rabelo, A. C.; Dalmaschio, C. J.; Pinheiro, A. N.; Pereira, E. C.; Schreiner, W. H.; Leite, E. R., *Adv. Energy Mater.* **2014,** *4* (6), 1301380.

39. Geng, X.; Zhang, Y.; Han, Y.; Li, J.; Yang, L.; Benamara, M.; Chen, L.; Zhu, H., *Nano Lett.* **2017,** *17* (3), 1825-1832.

40. Hu, B.; Qin, X.; Asiri, A. M.; Alamry, K. A.; Al-Youbi, A. O.; Sun, X., *Electrochim. Acta* **2013,** *100*, 24-28.

41. Liu, S.; Kim, K. H.; Yun, J. M.; Kundu, A.; Sankar, K. V.; Patil, U. M.; Ray, C.; Jun, S. C., *J. Mater. Chem. A* **2017,** *5* (13), 6292-6298.

42. Zhang, X.; Luo, J.; Tang, P.; Ye, X.; Peng, X.; Tang, H.; Sun, S.-G.; Fransaer, J., *Nano Energy* **2017,** *31*, 311-321.

43. Yu, X.; Lu, B.; Xu, Z., *Adv. Mater.* **2014,** *26* (7), 1044-1051.

44. Liang, H.; Xia, C.; Emwas, A.-H.; Anjum, D. H.; Miao, X.; Alshareef, H. N., *Nano Energy* **2018,** *49*, 155-162.

45. Liu, C.; Zhang, C.; Fu, H.; Nan, X.; Cao, G., *Adv. Energy Mater.* **2017,** *7* (1), 1601127.

46. Sun, T.; Li, Z.; Liu, X.; Ma, L.; Wang, J.; Yang, S., *J. Power Sources* **2016,** *331*, 180-188.

47. Krishnamoorthy, K.; Pazhamalai, P.; Veerasubramani, G. K.; Kim, S. J., *J. Power Sources* **2016,** *321*, 112-119.

48. Liu, S.; Lee, S. C.; Patil, U.; Shackery, I.; Kang, S.; Zhang, K.; Park, J. H.; Chung, K. Y.; Jun, S. C., *J. Mater. Chem. A* **2017,** *5*, 1043-1049.

49. Shi, Z.; Nie, K.; Shao, Z.-J.; Gao, B.; Lin, H.; Zhang, H.; Liu, B.; Wang, Y.; Zhang, Y.; Sun, X., *Energ Environ Sci.* **2017,** *10* (5), 1262-1271.

50. Yang, P.; Ding, Y.; Lin, Z.; Chen, Z.; Li, Y.; Qiang, P.; Ebrahimi, M.; Mai, W.; Wong, C. P.; Wang, Z. L., *Nano Lett.* **2014,** *14* (2), 731-736.

51. Gao, T.; Fjellvåg, H.; Norby, P., *Anal Chim Acta.* **2009,** *648* (2), 235-239.

52. Nakamoto, K.; Kano, Y.; Kitajou, A.; Okada, S., *J. Power Sources* **2016,** *327*, 327-332.

53. Niu, Z.; Zhou, W.; Chen, X.; Chen, J.; Xie, S., *Adv. Mater.* **2015,** *27* (39), 6002-6008.

54. Liu, Y.; Fu, N.; Zhang, G.; Xu, M.; Lu, W.; Zhou, L.; Huang, H., *Adv Funct Mater.* **2017,** *27* (8), 1605307.

55. Zhu, J.; Tang, S.; Wu, J.; Shi, X.; Zhu, B.; Meng, X., *Adv. Energy Mater.* **2017,** *7* (2), 1601234.

56. Liu, S.; Lee, S. C.; Patil, U. M.; Ray, C.; Sankar, K. V.; Zhang, K.; Kundu, A.; Park, J. H.; Jun, S. C., *J. Mater. Chem. A* **2017,** *5* (9), 4543-4549.

57. Liu, S.; Jun, S. C., *J. Power Sources* **2017,** *342*, 629-637.

58. Yang, X.; Zhao, L.; Lian, J., *J. Power Sources* **2017,** *343*, 373-382.

59. Masikhwa, T. M.; Madito, M. J.; Bello, A.; Dangbegnon, J. K.; Manyala, N., *J. Colloid Interface Sci.* **2017,** *488*, 155-165.

60. Wen, S.; Liu, Y.; Zhu, F.; Shao, R.; Xu, W., *Appl. Surf. Sci.* **2018,** *428*, 616-622.

61. Yang, X.; Niu, H.; Jiang, H.; Wang, Q.; Qu, F., *J. Mater. Chem. A* **2016,** *4* (29), 11264-11275.

62. Lee, T. H.; Pham, D. T.; Sahoo, R.; Seok, J.; Luu, T. H. T.; Lee, Y. H., *Energy Storage Mater.,* **2018,** *12*, 223-231.

63. Zhu, S.; Li, L.; Liu, J.; Wang, H.; Wang, T.; Zhang, Y.; Zhang, L.; Ruoff, R. S.; Dong, F., *ACS Nano* **2018,** *12* (2), 1033-1042.